Electrocatalytic reduction of carbon dioxide on gold–copper bimetallic nanoparticles: Effects of surface composition on selectivity

Mulatu Kassie Birhanu [a], Meng-Che Tsai [b,c], Chun-Tse Chen [a], Amaha Woldu Kahsay [a], Tamene Simachew Zeleke [a], Kassa Belay Ibrahim [b], Chen-Jui Huang [a], Yen-Fa Liao [d], Wei-Nien Su [b,c,*], Bing Joe Hwang [a,c,d,*]

[a] Department of Chemical Engineering, National Taiwan University of Science and Technology, Taipei 106, Taiwan
[b] Graduate Institute of Applied Science and Technology, National Taiwan University of Science and Technology, Taipei 106, Taiwan
[c] Sustainable Energy Development Center, National Taiwan University of Science and Technology, Taipei city 106, Taiwan
[d] National Synchrotron Radiation Research Center (NSRRC), Hsin-Chu 30076, Taiwan

ARTICLE INFO

ABSTRACT

In this work, bimetallic nanoparticles (NPs) of Au and Cu are synthesized for the electrochemical reduction reaction of CO_2 (CO_2RR). It is known that the binding strength between the reduction intermediates and the electrocatalyst affects the selectivity of products, but how to correlate the performance with the surface composition, structure, and properties of a bimetallic electrocatalyst, instead of stoichiometric or bulk composition remains less discussed. AuCu and $AuCu_3$ NPs with the size around ~8 nm were prepared. By excluding the size effect, the work studies the effects of surface composition and heteroatomic interaction on the selectivity and faradaic efficiency of the reduction products. Based on X-ray absorption spectroscopy (XAS), one can quantify the alloying extent and surface compositions of electrocatalysts, which are supposed to have the pivotal effects on the reaction pathways and the corresponding reduction products. It is found that high activity and notably improved CO selectivity of Au-Cu bimetallic NPs can be attributed to the heterometallic coordination and their electronic interactions. The reduction products were analyzed by gas chromatography and nuclear magnetic resonance (NMR) spectroscopy. Nearly 60 mA cm^{-2} of current density was recorded at -0.91 V vs. RHE, and selectivity of 78±4.3% CO was obtained using AuCu.

© 2020 Published by Elsevier Ltd.

1. Introduction

The global energy demand is continuously increasing. The majority of the energy depends on non-renewable resources especially fossils such as petroleum and crude oils. However, excess CO_2 is emitting to the atmosphere in the utilization of fossil fuels in various power plants, industries, vehicles, and other factories that can disrupt the environment and become a cause for global warming [1–7]. This challenging issue leads to an increase in temperature, unprecedented climate change, expansion of dissertation, acidification of oceans, and health effects [4, 8–11]. Therefore, remediation of emitted CO_2 is an important action before disseminating to the environment and affects the natural ecological system through the unbalancing carbon cycle [12–15]. Among many

remediation techniques, CO_2RR has plenty of advantages and it is a promising approach for the simultaneous development of green energy technology [4, 16, 17]. This is because it can be performed at ambient conditions, easily tuned by external parameters (such as potential, temperature, pressure, etc.) [13, 18–20], capable of producing valuable compounds like formate, carbon monoxide and other products. This type of reduction technique is a promising technology to provide in large scalability, to make an effective and efficient reduction of CO_2. Carbon monoxide can be reduced further into another compound containing high energy density, which can be used for green energy sources [15, 16, 20–23].

Although CO_2RR has numerous advantages, there are a few challenges affecting the faradaic efficiency and selectivity of products [5, 24–28]. Competitive hydrogen evolution reaction during CO_2 reduction that retards the reduction efficiency, and difficulties to separate products are challenges in the reduction process. Active sites of the surface perhaps blocked by reduction intermediates lead to deactivation of catalytic performance and shorten the lifetime of electrocatalyst, limited solubility and slow kinetics of CO_2

leads a weak mass transfer in the reduction process are also limitations of the process. Lastly, transfer and coupling of many electrons/protons, several reaction pathways, mechanisms [7, 27, 29–35], and many possible products make the process more complicated than other catalytic activities such as hydrogen evolution reaction (HER) [36, 37], oxygen evolution reaction (OER) [37–39] and oxygen reduction reaction (ORR) [24, 40–44].

Currently, bimetallic systems of electrocatalysts are preferable because of their versatility, optical properties over their single metal counterparts as well as lower energy utilization in the CO_2RR [28, 33, 39, 45–48]. Bimetallic electrocatalysts are able to tune the binding strength of the reduction intermediates of CO_2 and desorption of products by optimizing the surface composition, [33, 44, 49–51] analyzing the chemical properties and modifications of the composites. [47, 52–55] The preparation technique and modification of the surface can tune the synergistic effect between any two metals in the alloy formation. Among many bimetallic systems, alloys of Au and Cu have a great role in enhancing faradaic efficiency, improving the activity and selectivity of the CO_2RR. [27, 32, 42, 53, 56] Au-Cu alloys have been addressed by various researchers in a different aspect of the reduction process of CO_2 [5, 15, 39, 57–59].

Kim et al. [44] have studied the parameters that can enhance the turn over frequency of the reduction product and then dictates the selectivity and overall activity of the reduction process on Au-Cu NPs, which is prepared in a monolayer platform. In another study [60], this group has investigated the transformation of disordered to ordered atomic arrangement of AuCu nanoparticles (NPs). The ordered NPs are more selective towards the formation of CO than the disordered one. Chen et al. [25]. have synthesized coreshell Cu/Au nanostructure for electrochemical reduction of CO_2 to syngas with a stable CO/H_2 ratio at a potential −0.65 V vs. RHE. The result indicates Cu nanostructure generates a higher current density than polycrystalline Cu. Their result also showed the coating of a thin layer of Au on Cu nanowire enhances the FE% of CO.

Although binding strength between the electrocatalyst surface and reduction intermediates is known to have dominant roles in reaction mechanism and product selectivity, investigations reported in literature usually concern the relationship between the catalytic activity and composition. However, less attention has ever been given to the relationship between the catalytic activity and actual surface composition, e.g. in the case of a bimetallic electrocatalyst. Herein, we have synthesized bimetallic (AuCu & AuCu$_3$) and monometallic (Au & Cu) NPs supported on activated carbon nanotubes to address the above issues in detail by tuning the composition to understand the structural properties of electrocatalysts and to investigate the synergistic effects between Au and Cu. These features mainly analyzed by X-ray absorption near edge structure (XANES) and Extended X-ray absorption fine structure (EXAFS) including determination of the alloying extent and surface composition of atoms. The supported electrocatalysts were characterized by SEM, EDS, XRD, XPS and XAS to detect the morphology, composition, electronic properties and the structure of bimetallic NPs. The CO_2RR activity and selectivity of bimetallic electrocatalysts of Au and Cu were correlated with their surface composition, atomic coordination and interaction.

2. Experimental

2.1. Treatment of MWCNT

The type of carbon nanotubes used is Fullerene, multi-walled, ≤8 nm outer diameter, 2–5 nm internal diameter and 0.5–2 μm long. To treat and activate, 0.5 g of MWCNT (Alfa Aesar) was taken and calcinated at 500 °C for 5 h. Then it was cooled to room temperature mixed with 10% HCl (ACROS) and sonicated

for 30 min. Eventually, it was washed at least three times with ultra-pure water until pH of the washing solution was above 5. [61] The collected MWCNT was dried under vacuum at 60 °C followed by functionalizing it in acid and $KMnO_4$ based on the procedures, [62] which is described in detail in supportive information (Section 1 & Figure S1). Eventually, the functionalized MWCNT was characterized to confirm its property, morphology and purity. Finally, it is used as a supporting and activating material of the metal NPs for the catalysis activity in CO_2RR.

2.2. Preparation of metal nanoparticles supported on MWCNT

Electrocatalysts are prepared through the co-reduction process from the corresponding metal precursors using the procedure in Figure S2. To prepare AuCu/MWCNT/CP, 20 mL of 1-octadecene was heated at 130 °C in Ar environment for 30 min and 2 mmol of oleic acid, 2 mmol of oleylamine, 4 mmol of 1,2-hexadecanediol 3.33 mmol of treated MWCNT, 0.25 mmol of $CuCl_2•2H_2O$ (99%, ALDRICH) and 0.25 mmol of $HAuCl_4•3H_2O$ (99.99%, ALDRICH) were added to the reaction mixture. Under this inert environment, the mixture was heated to 200 °C with stirring for 2 h. Afterward, it was cooled to room temperature and ethanol was added followed by washing through centrifugation three times with ethanol and hexane consecutively. Finally, it was dried in vacuum at 60 °C then AuCu/MWCNT/CP was synthesized. In the same process and reaction condition to prepare AuCu$_3$/MWCNT/CP, 0.125 mmol of $HAuCl_4•3H_2O$ was used. To synthesize Au/MWCNT/CP and Cu/MWCNT/CP, 0.5 mmol of $HAuCl_4•3H_2O$ and 0.5 mmol of $CuCl_2•2H_2O$ were applicable respectively. The amount of MWCNT added in each composition was equal.

2.3. Electrochemical performance test and quantification of products

Cation exchange membrane (Nafion® 117, perfluorinated membrane, SIGMA ALDRICH) is commonly used to separate the anode and cathode in the H-cell reactor in which the reduction is performed at the cathode while oxidation takes place at anode [63–65] (Figure S3). The main purpose of the membrane is to transport the charge carriers and to prevent the crossover of reduction intermediates and final reduction products between the anode and cathode compartments. [65, 66] Three electrode system i.e. Ag/AgCl (3 M) and Pt wire are used as reference and counter electrode respectively. The electrocatalysts deposited on carbon paper (AuCu/MWCNT/CP, AuCu$_3$/MWCNT/CP, Au/MWCNT/CP & Cu/MWCNT/CP) are used as a working electrode in 0.5 M of $KHCO_3$ (99.7%, ALDRICH) electrolyte solution with pH value 8.3. Before the electrochemical test, the solution was saturated with Ar and CO_2 by purging for 30 min at a rate of 100 mL min^{-1}. Cyclic voltammetry (CV) and linear sweep voltammetry (LSV) analysis were performed within the potential domain of 0.38 V to −1.1 V vs. RHE in Ar and CO_2 environment to test the performance of the reduction activity. The pH of the solution after electrolysis was measured and recorded in between 7.8 to 8.1, depending on the product type formed using each electrocatalyst.

The electrocatalyst slurry was prepared by dissolving 10 mg of each electrocatalyst with 1 mL mixture of isopropanol, absolute ethanol, ultra-pure water and an appropriate amount of Nafion solution [67] (5% Nafion, SIGMA ALDRICH), which is used as a binder to tightly deposit metal nanoparticles [68] and multi-walled carbon nanotubes on the carbon paper. After sonication and complete dissolution of the slurry, 72 μL of each composition was dispersed on 1 cm^2 carbon paper and dried at room temperature for 3–5 h.

Electrochemical impedance spectroscopy (EIS) was measured at −0.91 V vs. RHE at a frequency range between 100k Hz–0.1 Hz and an amplitude of 10 mV for 50 cycles. The stability of each

electrocatalyst was measured at a specific potential for 3 h. The reduction of CO_2 was performed through chronoamperometry at −0.51 V, −0.71 V and −0.91 V vs. RHE. The reduction process was carried out in our laboratory designed electrochemical reactor cell which is connected with GC via a continuous flow of CO_2 (10 mL min^{-1}) into the reactor cell containing the electrolyte solution. After CO_2RR through the designed configuration and set up, gaseous products (CO and H_2) were detected and quantifiable directly by online gas chromatography (GC), while the liquid parts were determined by offline nuclear magnetic resonance (NMR) spectroscopy. To quantify CO and H_2, calibration curves were constructed using known concentrations of each standard gas. Quantification of HCOOH was conducted using a specified amount dimethylsulfoxide (DMSO), which is used as a reference/standard in NMR analysis for calibration via deconvolution of the standard peaks by Topspin software.

2.4. Determination of alloying extent and surface composition using XAS

The atomic distribution, alloying extent and surface composition of bimetallic NPs can be evaluated by deriving structural parameters of XAS. The basic parameters needed to determine alloying extent are P$_{random}$ (P$_{ra}$), R$_{random}$ (R$_{ra}$), P$_{observed}$ (P$_{ob}$), and R$_{observed}$ (R$_{ob}$) in which P$_{random}$ and R$_{random}$ obtained from XAS analysis. Mathematically, it is expressed as P$_{observed}$=N$_{Au-Cu}$/ΣN$_{Au-i}$, R$_{observed}$=N$_{Cu-Au}$/ΣN$_{Cu-i}$. P$_{observed}$ is justified as the ratio of the scattering atoms of Cu coordination number around absorbing atoms of Au (N$_{Au-Cu}$) to the total coordination number of absorbing atoms (ΣN$_{Au-i}$). In the same way, R$_{observed}$ is described as the ratio of the scattering atoms of Au coordination number around absorbing atoms of Cu (N$_{Cu-Au}$) to the total coordination number of absorbing atoms (ΣN$_{Cu-i}$). Therefore, according to the above principle, the alloying extents of Au and Cu (J$_{Au}$ and J$_{Cu}$) are determined using Eq. (1) & 2 respectively [7, 69].

$$J_{Au} = \frac{P_{observed}}{P_{random}} \times 100\% \qquad (1)$$

$$J_{Cu} = \frac{R_{observed}}{R_{random}} \times 100\% \qquad (2)$$

The surface composition of Au is analyzed based on the following mathematical expression (Eq. (3)) [70].

$$X^s(Au) = \frac{x(\sum N_{Au-i} - 12)}{x(\sum N_{Au-i} - 12) + (1-x)(\sum N_{Cu-i} - 12)} \qquad (3)$$

where; X^s(Au) is the surface compositions of Au, x represents bulk composition obtained from Au L3-edge jump. The nomenclature to describe the parameters and symbols in XAS measurement are shown in Table S4. The apparatus and instrument details for all experiment in this work is described in supportive information Section 12.

3. Results and discussion

3.1. Characterization of electrocatalysts

The dispersion of metal NPs on the carbon nanotubes is clearly observed by advanced SEM measurement (Fig. 1& Figure S4). The SEM image reveals not only the availability of metals but also it shows the uniformity of metal NPs on the supporting material (MWCNT). The SEM images and energy dispersive X-ray spectroscopy (EDS) mappings in Fig. 1 reveal that the metal NPs are detected and uniformly distributed on MWCNT. The morphology of bare MWCNT is observed using SEM image as shown in Fig. 1a while Fig. 1b depicts the dispersion of AuCu alloy on MWCNT. Elemental mappings of Au, Cu and C in AuCu/MWCNT shown in
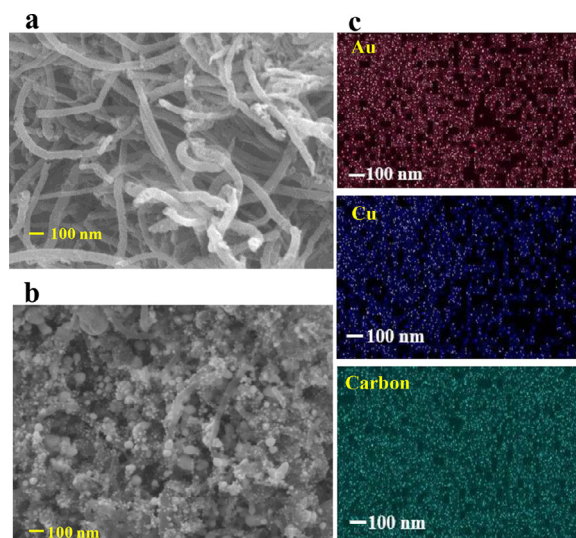

Fig. 1. The SEM images of (a) MWCNT without metal nanoparticles, (b) AuCu/MWCNT, (c) EDS elemental maps of Au, Cu and carbon in AuCu/MWCNT.
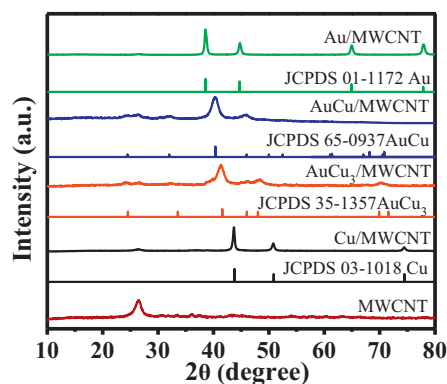

Fig. 2. XRD patterns of monometallic electrocatalysts (Au/MWCNT & Cu/MWCNT) and the bimetallic (AuCu/MWCNT & AuCu$_3$/MWCNT) nanoparticles.

Fig. 1c confirm the uniform distribution of each element in the electrocatalyst.

The composition of each metal NP in bimetallic and monometallic is confirmed using a number of techniques. XRD pattern of each NP including MWCNT (Fig. 2) matches with the corresponding characteristic pattern (JCPDS file) of each phase, which was recorded in the range of 10≤2θ≤80°. Major peaks of the intermetallic type alloy i.e. AuCu/MWCNT and AuCu$_3$/MWCNT appeared at 40.31° and 41.28° respectively, which are found in between the major peaks of monometallic i.e. Au (2θ=38.54°) and Cu (2θ=43.67°). The significant peak shift is observed in bimetallic NPs compared to monometallic that confirms the appearance of a new phase due to the formation of an alloy [71]. The XRD pattern also indicates the particle size of bimetallic NP (~8 nm) is lower compared to the size of NPs of the individual metal (~12–13 nm). The weight percent and bulk composition of each atom in the bimetallic are determined by EDS measurement as reported in Figure S5, while the surface chemistry of each electrocatalyst was further investigated by XPS analysis.

Functionalizing MWCNT with acids and oxidizing agents can enhance the chemical reactivity typically through the formation of carboxyl and hydroxyls as it is confirmed by XPS measurement and fitting. The wide scan surveys for XPS measurement for each composition (AuCu/MWCNT, AuCu$_3$/MWCNT, Au/MWCNT & Cu/MWCNT) are shown in Fig. S6 (a-d) respectively. In the
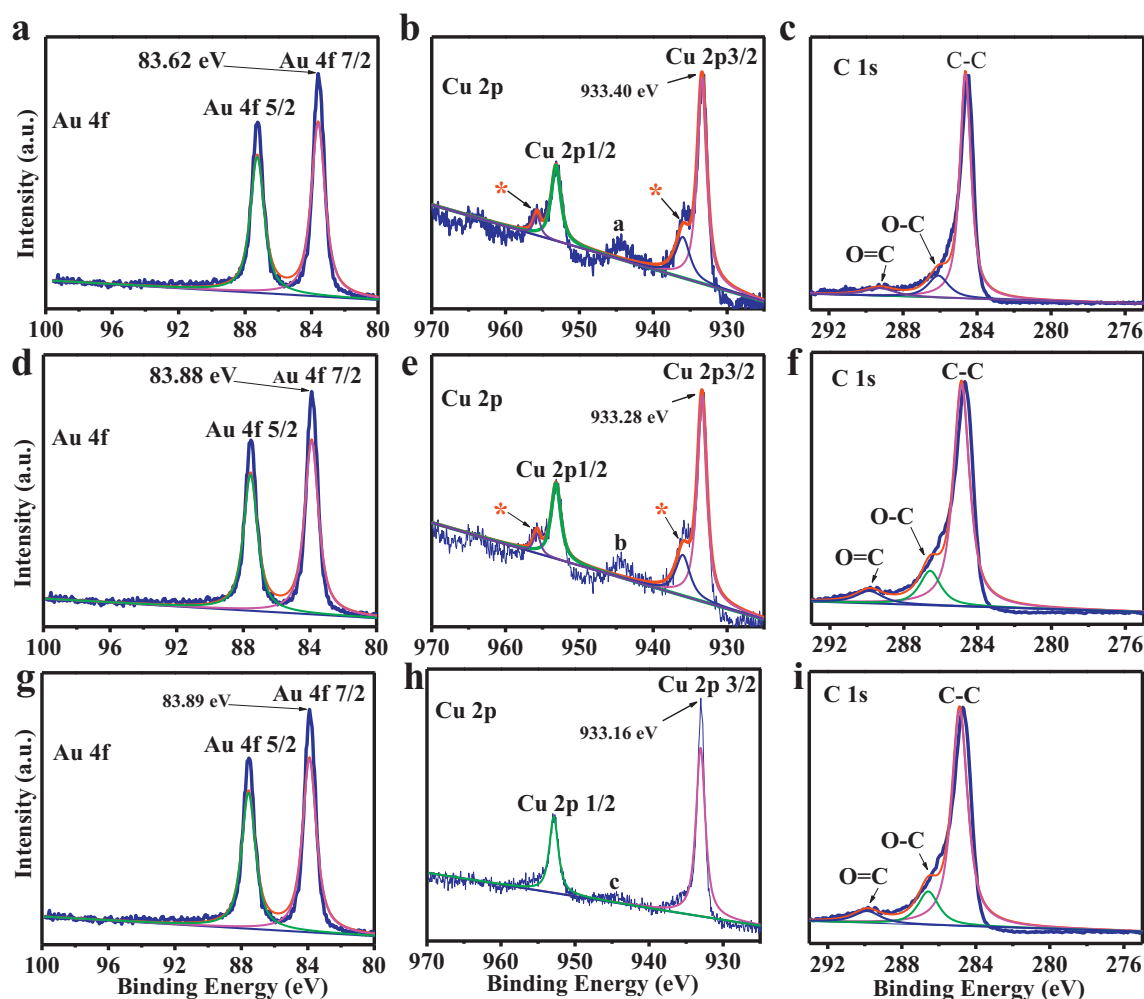
Fig. 3. XPS spectra for monometallic catalyst (a) Au 4f region in Au/MWCNT, (b) Cu 2p region in Cu/MWCNT and (c) C 1 s region in Au/MWCNT; XPS spectra of bimetallic (d) Au 4f region (e) Cu 2p region and (f) C 1 s region in AuCu₃/MWCNT, (g) Au 4f region, (h) Cu 2p region and (i) C 1 s region in AuCu/MWCNT. (The pink indicates the fitting line for the peaks Au 4f 7/2, Cu 2p 3/2 and C–C region in C 1 s, the green one shows the fitting line for 4f 5/2 and Cu 2p 1/2 peak, the red is the peak sum and the blue represents the raw data).

XPS measurements, the atomic ratio (%) of Au, Cu and C in AuCu/MWCNT are 6.7%, 5.4% and 87.9% while in AuCu₃/MWCNT it is obtained 2.9%, 10.3% and 86.8% respectively as shown in Table S1. These values are higher than the atomic ratio obtained using EDS analysis. This indicates that metal NPs are present mainly on the surface part of the electrocatalysts loading the carbon nanotubes.

In monometallic NPs, the XPS spectrum shown in Fig. 3a represents Au 4f regions i.e. Au 4f 5/2 & Au 4f 7/2, while Fig. 3b reveals Cu 2p orbital regions i.e. Cu 2p1/2 & Cu 2p3/2. The spectrum of C 1 s region in Au/MWCNT is shown in Fig. 3c. In bimetallic AuCu₃/MWCNT and AuCu/MWCNT, all spectra of Au 4f, Cu 2p and C 1 s region are shown in Fig. 3 (d-f) and Fig. 3 (g-i) respectively. The binding energy of Au 4f spectra in the bimetallic is shifted to a higher value from 83.62 eV to 83.89 eV, while Cu 2p orbitals shifted slightly to the right (lower binding energy) compared to monometallic. This indicates there is electron transfer from Au to Cu in AuCu₃/MWCNT and AuCu/MWCNT. In all electrocatalysts, the smaller spectrum in C1s region appeared on the left side of C–C sp3 peak due to O = C & O–C groups, which were caused by functionalizing the carbon nanotubes. The shoulders XPS peaks in Cu 2p region (Fig. 3b & 3e) for AuCu₃/MWCNT and Cu/MWCNT respectively, indicated by the red star are due to the formation of minor hydroxides on the Cu surface arising from the incorporation of oxygen on Cu during the measurement and/or transporta-

tion of samples in XPS. This is because Cu NP is sensitive to react with air/oxygen and has a tendency to form hydroxide or oxide. However, this phenomenon was not observed in AuCu/MWCNT. The reason might be less amount of Cu was present in this composition compared to AuCu₃/MWCNT and Cu/MWCNT. The peaks ;abelled as "a", "b" & "c" might be satellites (shake-off and shake-up) peaks due to a sudden change in columbic potential as the photon ejected electron passing through the valence band [75–77].

The presence of oxygen-containing groups on it facilitates the exfoliation of MWCNT bundles and increases the solubility in polar media [72–74]. The atomic ratio of oxygen is not reported because it is expected the source of oxygen was not from the sample rather due to exposed with air during measurement. This scenario is confirmed using a better sensitive technique i.e. XAS analysis, where no oxidation of samples was observed.

3.2. Investigations of properties of electrocatalysts using XAS

The XANES spectra give information about the oxidation state and electronic environment of the absorbing atom, while the EX-AFS spectra provide information on the type, number and distance of the backscattering atom surrounding the central atom and provide geometric information [69]. Fig. 4a reveals XANES spectra of Cu K-edge of samples with the corresponding metal reference. In
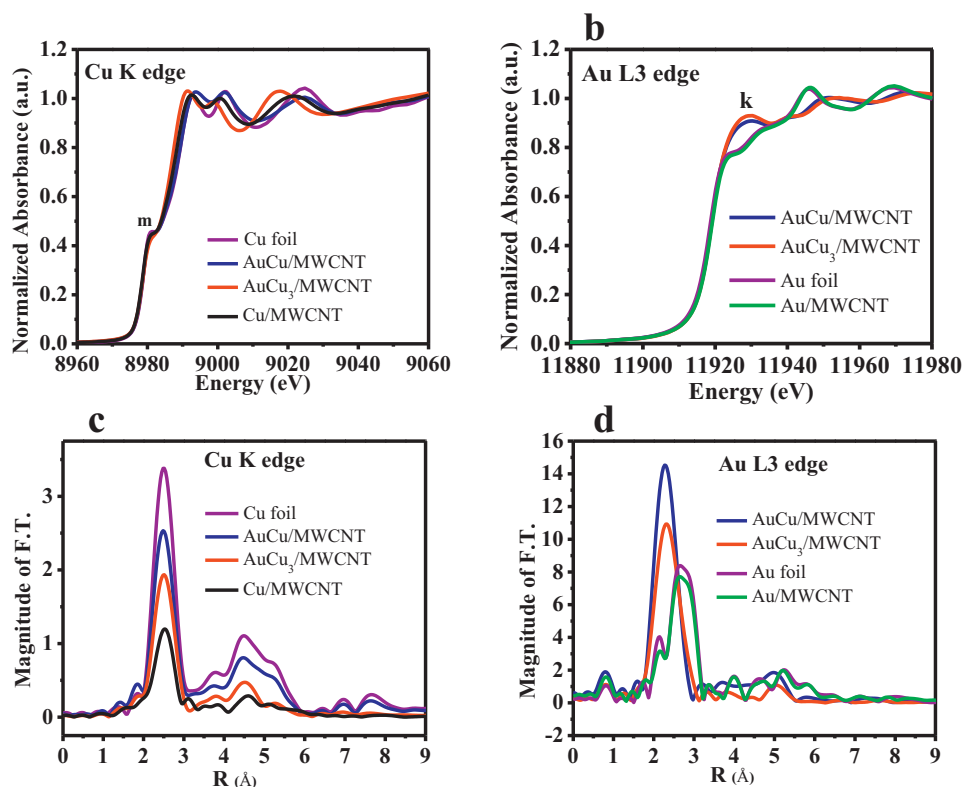
Fig. 4. XANES spectra (a) Cu K-edge and (b) Au L3-edge; EXAFS data of (c) Cu K-edge, and (d) Au L3-edge in AuCu/MWCNT, AuCu$_3$/MWCNT, Au/MWCNT and Cu/MWCNT.

all samples, the appearance of a more intense peak (peak "m") is ascribed to the transition of 1 s to 4p$_{xy}$ in Cu atom. Furthermore, the oxidation state of Cu in AuCu/MWCNT and AuCu$_3$/MWCNT was found almost identical to the bulk reference i.e. Cu foil. In XANES of Au L3-edge (Fig. 4b), the energy was similar for all samples. The oxidation state of Au in bimetallic samples was close to the metallic state in the reference i.e. Au foil. These pieces of evidence show that the bimetallic samples were free of oxide. Furthermore, it is to note that the symbol '**k**' denotes the difference of white line intensity of bimetallic samples to the monometallic ones, indicating that Au in these samples possesses higher unfilled electron states than Au foil and Au/MWCNT. This implies electron transfer between Au and Cu in bimetallic samples. The change in electronic properties will also affect their catalytic features.

EXAFS gives information about the bonding distances, the co-ordination environment of an atom of interest and others [69]. Herein, the EXAFS analysis was used to investigate the formation of homo and heteroatomic interactions between metal NPs including the quantifications and type of atoms present surrounding the central atom, which is described in terms of coordination number and alloying extent. EXAFS fittings of Au L3 and Cu K-edges including K-space are shown at supporting files in Figure S7 & S8. Their fitting parameters are reported and elaborated in Table 1. Spectra of Cu K-edge in Cu/MWCNT, AuCu/MWCNT and AuCu$_3$/MWCNT depict the formation of Cu-Cu and Cu-Au bonds (Fig. 4c) involving Cu is the central atom. In EXAFS of Au L3-edge in Fig. 4d, Au-Cu and Au-Au are the bonds existing in the bimetallic electrocatalyst involving Au is the central atom surrounded by Cu and other Au atoms. The bimetallic NP exhibits higher first shell scattering amplitude than Au foil and Au/MWCNT. This belongs to the stronger constructive interference of photoelectron scattering in the ordered structural clusters surrounding Au. The intensive amplitude and shorter bond length of Au-Cu in AuCu/MWCNT and AuCu$_3$/MWCNT ascribable to the alloying and synergistic effect between the two atoms. This

alteration in structural and electronic properties of atoms in the bimetallic samples is the main electronic parameter enhancing the catalytic ability of the electrocatalysts.

Resolving the backscattered wavelets, the structural features, e.g. the neighboring coordination and bonding configuration of the absorbing atom can be determined. The total coordination number of each metal is less than that of the corresponding metal foil and confirms the presence of uncoordinated atom that can attribute enhancement of the catalytic activity in addition to the strong synergistic effect (electronic and geometric) of Au-Cu bond. The variation of coordination number and effect of surrounding atoms (geometric effect) and the detailed information about XAS measurement is reported in the fitting results shown in the table. The table elaborates the coordination number of Au-Au in AuCu/MWCNT and AuCu$_3$/MWCNT are 5.72±1.24 and 1.16±0.12 respectively. This value indicates that Au is surrounded by many Au atoms in AuCu/MWCNT, compared to AuCu$_3$/MWCNT where the Au atoms in AuCu$_3$ are largely surrounded by Cu atoms. The coordination number of Cu-Cu in AuCu/MWCNT and AuCu$_3$ are 7.44±1.40 and 6.96±0.34 respectively. This implies Cu is surrounded by more Cu and less Au atoms, because the coordination number of Cu-Au in AuCu/MWCNT and AuCu$_3$/MWCNT are 3.35±1.10 and 1.74±0.32 respectively. The coordination structures will be further correlated with the estimated surface composition analysis using XAS data, as shown in Table 2 in Section 3.3.

3.3. Quantitative determination of alloying extent and surface composition

In addition to the above discussion of XANES and EXAFS, XAS results can reveal information such as the alloying extent (J) and surface composition of bimetallic NPs. Hwang et al. [69]. have designed the alloying extent model for bimetallic using seven alternatives of atomic distribution based on Eqs. (1) and (2). Referring

Table 1

The curve fitting results of Au L3-edge and Cu K-edge for monometallic, bimetallic and corresponding metal foils of Au and Cu.

Sample	Shell	N[a]	R [Å][b]	ΔE_0 [eV] [c]	σ^2 [Å²][d]	R-factor[e] ($\times 10^{-2}$)
AuCu/MWCNT	Au-Au	5.72±1.24	2.79±0.05	4.51±1.88	0.013	0.1
	Au-Cu	5.82±1.10	2.66±0.02		0.009	
	Cu-Au	3.35±1.10	2.66±0.02		0.019	
	Cu-Cu	7.44±1.40	2.54±0.01		0.008	
AuCu₃/MWCNT	Au-Au	1.16±0.12	3.04±0.16	2.99±0.52	0.009	0.13
	Au-Cu	9.86±0.32	2.63±0.01		0.009	
	Cu-Au	1.74±0.32	2.63±0.01		0.011	
	Cu-Cu	6.96±0.34	2.56±0.01		0.011	
Au/MWCNT	Au-Au	11.20±0.62	2.86±0.01	4.11±0.39	0.008	0.18
Au foil	Au-Au	12.0 ± 0.36	2.86±0.01	4.66±0.22	0.008	0.07
Cu foil	Cu-Cu	12.0 ± 0.79	2.54±0.01	4.02±0.69	0.009	

[a] Coordination numbers, [b] Bond length, [c] Inner potential shift, [d] The Debye-Waller factor, [e] Running factor.

Table 2

XAS measurement parameters and results in estimating alloying extent and surface composition of Au and Cu in the bimetallic AuCu and AuCu₃ electrocatalysts.

Sample	ΣN_{Au-i}	ΣN_{Cu-i}	$P_{observed}$	P_{random}	$R_{observed}$	R_{random}	J_{Au}	J_{Cu}	$X^s(Au)$
AuCu/MWCNT	11.54	10.79	0.50	0.50	0.40	0.50	100	80	0.61
AuCu₃/MWCNT	11.02	8.70	0.89	0.75	0.41	0.25	119	160	0.23

to the same methodology, the bimetallic alloying extent values for Au and Cu in AuCu/MWCNT were calculated as $J_{Au} = 100\%$ and $J_{Cu} = 80\%$. In this case, Au atoms prefer Cu rather than Au, but Cu atoms prefer Cu rather than Au during the formation of an alloy. For this reason, the distribution of Au is significantly better than that of Cu atoms because J_{Au} is greater than J_{Cu}. Therefore, at the equilibrium state, the interactions (H) are compared as follows: $H_{Cu-Cu} > H_{Au-Cu} > H_{Au-Au}$. For this type of scenario, NPs of the alloy favor a structure similar to that of the Cu rich in core and Au rich in the shell. [35, 44, 78] In the case of AuCu₃, the alloying extent of Au and Cu are $J_{Au} = 119\%$ and $J_{Cu} = 160\%$ respectively. In this condition, it describes that heteroatomic interaction is more intensive than homoatomic, however, the amount of Au atom in the shell is lower on AuCu₃/MWCNT/CP.

Additionally, the surface compositions of Au, $X^s(Au)$, relative to Cu in AuCu/MWCNT and AuCu₃/MWCNT were evaluated using Eq. (3). The parameters and results are reported in Table 2. Actual surface composition is very important because the selectivity of products is related to the types of atoms present on the surface of the electrocatalyst and sometimes related to the size of metal NPs. The calculated Au composition on the surface of AuCu/MWCNT is 0.61, much higher than the bulk or stoichiometric composition (0.5). Additionally, the calculated Au composition on the surface of AuCu₃/MWCNT is 0.23, slightly lower than the bulk or stoichiometric composition (0.25). It is to address that the surface and bulk compositions of bimetallic NPs could be different, as demonstrated in the aforementioned EXAFS analysis and calculations.

3.4. The performance of electrochemical reduction of CO_2

The performance of CO_2RR using electrocatalysts and MWCNT/CP was tested by LSV in potential domain −1.1 V to 0.38 V vs. RHE in 0.5 M KHCO₃ (pH=8.3) after saturated with CO_2 (Fig. 5a) and in Ar environment (Figure S9b). The amount of current produced in CO_2 environment was significantly higher than in Ar saturated solution. Because there is no CO_2 reduction in the latter case. The increment of current in CO_2 environment indicates the progression of CO_2 reduction. The reduction activity using AuCu/MWCNT/CP is highest compared to other compositions. Since the surface area of each electrocatalyst is nearly the same (Table S3), it is possible to claim that the activity difference among electrocatalysts arises from the homo and heteroatomic interactions between Au and Cu in the alloy. Electrochemical

impedance was performed at an amplitude of 10 mV and a frequency range of 10 kHz–10 mHz for 50 cycles during CO_2RR at −0.91 V vs. RHE. The total resistance of AuCu/MWCNT/CP is ~10 Ω, which is the least resistance value compared to the resistance obtained in AuCu₃/MWCNT/CP and monometallic (Fig. 5b). This phenomenon is related to the electrocatalytic performance of each electrocatalyst. In all impedance measurements, the solution resistance (Rs) was very small due to the high concentration of the electrolyte solution (0.5 M KHCO₃) that increased greatly the ionic conductivity. Thus, the IR drop compensation was considered based on the Rs value. Comparing Fig. 5a and Figure S9a, the highly conductive MWCNT plays a role in enhanced performance.

The electrochemical result shows that AuCu/MWCNT/CP shows the highest reduction performance and it has the least charge transfer resistance. It is interesting to note that both bimetallic electrocatalysts exhibit better activity than their monometallic counterparts. This can be first ascribed to the synergy created by the heteroatomic coordination of Au and Cu atoms and the composition on the surface, as estimated by the XAS measurements. Furthermore, the unsaturated coordination numbers for Au and Cu indicate that these vacancy sites could be the additional active sites [37, 43, 79].

The stability of each electrocatalyst was tested through chronoamperometry at −0.91 V vs. RHE for 3 h. The result indicates all catalysts are stable enough for CO_2RR (Fig. 6). The trends of recorded current density generated by all samples is identical to the order shown in LSV measurements. The use of the high surface of MWCNT is believed to enable better dispersion of electrocatalysts and endow them with good durability.

3.5. Determination of the reduction products in CO_2RR

CO_2RR was performed in a reactor that was connected to the gas chromatography (GC) with a continuous flow of CO_2 (10 mL/minute) feed into the cathode compartment containing an electrolyte solution. The experimental steps/flows are demonstrated in Figure S10, and the instrumental details are mentioned in supportive information section 12. In GC analysis with the determination scope of quantifying CO and H_2, the reduced gas passed through the inlet of GC and entered into the column together with a carrier gas (helium). The quantification of reduced gases was determined by establishing calibration curves from standards of CO and H_2 (Figure S11, S12 & S13), while formate was quantified by
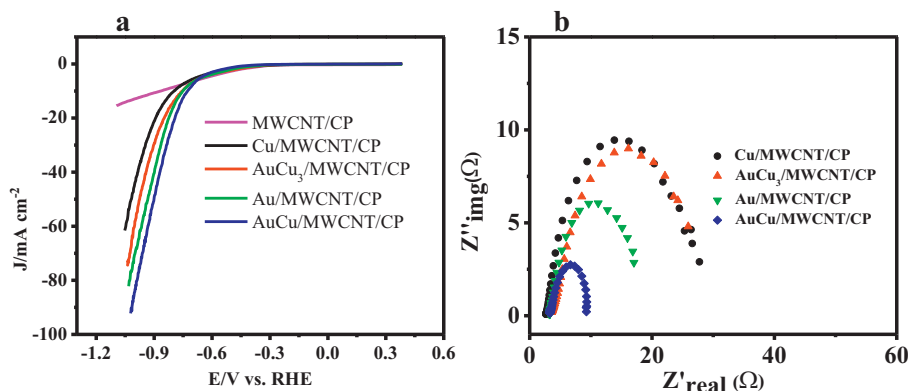
Fig. 5. (a) Linear sweep voltammetry (LSV) of CO_2RR using electrocatalysts and MWCNT/CP, (b) The Nyquist plots in electrochemical impedance measurement for each electrocatalyst at −0.91 V vs. RHE in 0.5 M $KHCO_3$ saturated in CO_2.
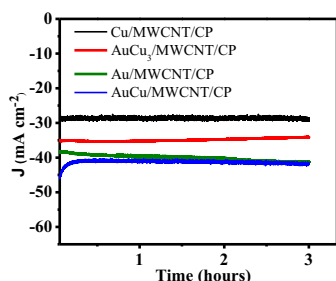

Fig. 6. Stability test of electrocatalysts during CO_2RR through chronoamperometry at −0.91 V vs. RHE in 0.5 M $KHCO_3$, which was saturated with CO_2.
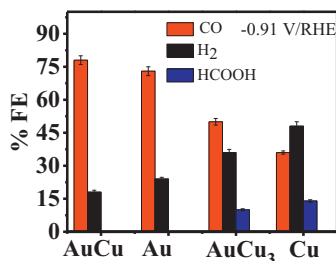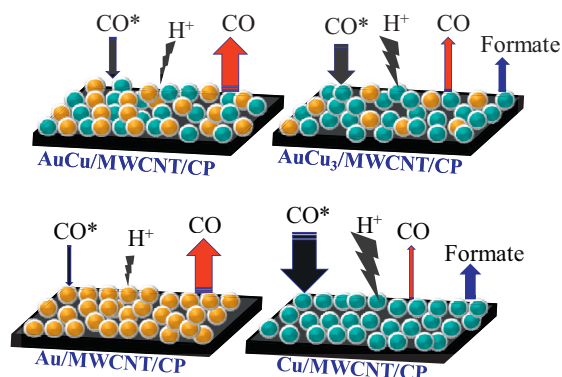

Fig. 7. Faradaic efficiencies of AuCu/MWCNT/CP, Au/MWCNT/CP, $AuCu_3$/MWCNT/CP and Cu/MWCNT/CP at −0.91 V vs. RHE in 0.5 M $KHCO_3$.

Scheme 1. Schematic demonstrations of the binding strength of CO* and H_2, including the desorption status of reduction products from the surfaces of each electrocatalyst. The thickness of all arrows indicates the relative adsorption and desorption strength of reaction intermediates and reduction products. Downward arrows towards the electrocatalyst surface refer to adsorption strength, while the upward arrows show the desorption ability of products.

3.6. Correlation between catalytic activity and surface properties of electrocatalysts

According to the results above and knowledge from literature, this section is focused on relating the catalytic activity and product distribution with the surface properties of the electrocatalysts. Published articles reported that the approximate binding strength between Au and CO* is nearly −0.3 eV while Cu and CO* is about −0.7 eV indicates the strength of CO* with Au is weaker than that of Cu [32, 35, 44, 78, 80–82]. Scheme 1 demonstrates the interaction between the reaction intermediates and the surfaces of electrocatalysts. The information is schemed by considering Au and Cu's properties attributing from DFT results in the literature and our previous article [35, 83]. The scheme shows that each composition has different binding strength with the reduction intermediates (CO* & hydrogen) and desorption tendency with products.

In this study, the enhanced activity and selectivity of CO_2RR on AuCu/MWCNT/CP towards CO is attributed to the enrichment of Au on the surface and the interaction between Au and Cu. The Au-rich surface has weaker binding strength between the surface and CO* that leads to easier desorption of CO from the surface. The effect of heterometallic interaction is also confirmed by comparing the FE% of CO between AuCu/MWCNT/CP and Au/MWCNT/CP, where the bimetallic generates higher CO by suppressing evolution of hydrogen compared to the monometallic. In contrast, Cu or Cu-rich electrocatalysts have stronger binding interaction with

NMR (Figure S14). In the evaluation of the reduction performance, FE% of each product depends on the composition of electrocatalysts, as seen in Fig. 7. The FE% of CO using AuCu/MWCNT/CP at −0.91 V vs. RHE is 78±4.3%. The amount of FE% of CO at the indicated potential using Cu/MWCNT/CP and Au/MWCNT/CP was 36±2.8% and 73±4.0% respectively even though the FE% of CO using Au/MWCNT/CP is higher than $AuCu_3$/MWCNT/CP. Formate was also detected using Cu/MWCNT/CP and $AuCu_3$/MWCNT/CP with FE% of 14±1.5% and 10±1.2% respectively at −0.91 V vs. RHE.

Comparing these two electrocatalysts ($AuCu_3$ vs. Cu), one can find the alloy also able to suppress the competitive H_2 evolution reaction. At lower potentials (−0.71 V & −0.51 V vs. RHE), the FE% of CO is decreased, and that of H_2 is increased compared to its FE% at −0.91 V vs. RHE as shown in Figure S15. The current density and FE% of CO in this work are compared with literature values as summarized in Table S2, and it shows the presence of MWCNT boosts the reduction activity. The enhancement effect of MWCNT in bimetallic is better than the corresponding monometallic. The reason might be that the bimetallic NPs have smaller particle sizes, which increases the coupling effect with MWCNT.

intermediates, and the slow desorption of CO favors the formation of formate. This phenomenon accounts for lower FE% of CO using Cu/MWCNT/CP and $AuCu_3$/MWCNT/CP compared to Au-rich electrocatalysts.

4. Conclusion

Tuning the surface composition and the structure of the Au-Cu bimetallic electrocatalysts affects the catalytic activity and selectivity of CO_2RR. The heteroatomic interaction between Au and Cu is evaluated by calculating the alloying extent of each atom that can determine the surface properties of the electrocatalyst. The alloying extent of Au and Cu in AuCu and $AuCu_3$ are 100% and 80%, respectively. These values indicate the existence of the interaction between the atoms, which contributes for the enhancement of CO_2RR. Additionally, the value of the alloying extent of Au in AuCu specifies the surface is rich in Au related to Cu. Since the binding strength between the Au surface and the reduction intermediate (CO*) is low, the desorption rate of the product (CO) is high. Thus, AuCu/MWCNT/CP is more selective towards CO (~78 FE%). On the other hand, the formation of CO on $AuCu_3$/MWCNT/CT is less compared to AuCu/MWCNT/CT due to the surface is rich in Cu. Therefore, the high binding strength of CO* with Cu-rich surface in $AuCu_3$/MWCNT/CT and Cu/MWCNT/CT favors retaining the reduction intermediates on the surface to produce formate. Finally, it is concluded that the activity and selectivity of CO_2RR on the Au-Cu bimetallic electrocatalysts depend on the surface composition and interaction of the atoms.

Declaration of Competing Interest

The authors declare that they have no known competing financial interests or personal relationships that could have appeared to influence the work reported in this paper.

CRediT authorship contribution statement

Mulatu Kassie Birhanu: Investigation, Formal analysis, Data curation, Writing - original draft. **Meng-Che Tsai:** Investigation, Data curation. **Chun-Tse Chen:** Investigation. **Amaha Woldu Kahsay:** Investigation. **Tamene Simachew Zeleke:** Investigation. **Kassa Belay Ibrahim:** Investigation. **Chen-Jui Huang:** Investigation, Data curation. **Yen-Fa Liao:** Investigation. **Wei-Nien Su:** Methodology, Visualization, Writing - review & editing, Supervision. **Bing Joe Hwang:** Conceptualization, Project administration, Supervision, Writing - review & editing, Resources.

Acknowledgement

Supplementary materials

Supplementary material associated with this article can be found, in the online version, at doi:10.1016/j.electacta.2020.136756.

Reference

[1] G.A. Florides, P. Christodoulides, Global warming and carbon dioxide through sciences, Environ. Int. 35 (2009) 390–401.

[2] J. Hansen, M. Sato, R. Ruedy, A. Lacis, V. Oinas, Global warming in the twenty-first century: an alternative scenario, Proc. Natl. Acad. Sci. U S A 97 (2000) 9875–9880.

[3] R.G. Williams, V. Roussenov, P. Goodwin, L. Resplandy, L. Bopp, Sensitivity of global warming to carbon emissions: effects of heat and carbon uptake in a suite of earth system models, J. Clim. 30 (2017) 9343–9363.

[4] H.B. Yang, S.-F. Hung, S. Liu, K. Yuan, S. Miao, L. Zhang, X. Huang, H.-Y. Wang, W. Cai, R. Chen, J. Gao, X. Yang, W. Chen, Y. Huang, H.M. Chen, C.M. Li, T. Zhang, B. Liu, Atomically dispersed Ni(i) as the active site for electrochemical CO_2 reduction, Nat. Energy 3 (2018) 140–147.

[5] N.S.R. Cuellar, O. Hinrichsen, M. Fleischer, Electrochemical reduction of CO_2 in water-based electrolytes $KHCO_3$ and K_2SO_4 using boron doped diamond electrodes, Chemistry Select 3 (2018) 3591–3595.

[6] K.J. Samira Siahrostami, Mohammadreza Karamad, Karen Chan, Haotian Wang, Jens Nørskov, Theoretical Investigations into Defected Graphene for Electrochemical Reduction of CO_2 ACS Sustainable Chem, Eng. 5 (2017) 11080–11085.

[7] M.E.S. Chiara Genovese, Emma K. Gibson, Diego Gianolio, Victor Posligua, Ricardo Grau-Crespo, Giannantonio Cibin, Peter P. Wells, Debi Garai, Vladyslav Solokha, Sandra Krick Calderon, Juan J. Velasco-Velez, Claudio Ampelli, Siglinda Perathoner, Georg Held, Gabriele Centi&, Rosa Arrigo, Operando spectroscopy study of the carbon dioxide electro-reduction by iron species on nitrogen-doped carbon, Nat. Commun. 9 (2018) 1–12.

[8] M.S. Dresselhaus, I.L. Thomas, Alternative energy technologies, Nature 414 (2001) 332.

[9] K.P. Kuhl, E.R. Cave, D.N. Abram, T.F. Jaramillo, New insights into the electrochemical reduction of carbon dioxide on metallic copper surfaces, Energy Environ. Sci. 5 (2012) 7050–7059.

[10] G.A. Ozin, Throwing new light on the reduction of CO_2, Adv. Mater. 27 (2015) 1957–1963.

[11] J.D. Shakun, P.U. Clark, F. He, S.A. Marcott, A.C. Mix, Z. Liu, B. Otto-Bliesner, A. Schmittner, E. Bard, Global warming preceded by increasing carbon dioxide concentrations during the last deglaciation, Nature 484 (2012) 49–54.

[12] F.S. Roberts, K.P. Kuhl, A. Nilsson, High selectivity for ethylene from carbon dioxide reduction over copper nanocube electrocatalysts, Angew. Chem. Int. Ed. 54 (2015) 5179–5182.

[13] M. Gattrell, N. Gupta, A. Co, A review of the aqueous electrochemical reduction of CO_2 to hydrocarbons at copper, J. Electroanal. Chem. 594 (2006) 1–19.

[14] J. Shen, R. Kortlever, R. Kas, Y.Y. Birdja, O. Diaz-Morales, Y. Kwon, I. Ledezma-Yanez, K.J.P. Schouten, G. Mul, M.T. Koper, Electrocatalytic reduction of carbon dioxide to carbon monoxide and methane at an immobilized cobalt protoporphyrin, Nat. Commun. 6 (2015) 8177.

[15] W. Tang, A.A. Peterson, A.S. Varela, Z.P. Jovanov, L. Bech, W.J. Durand, S. Dahl, J.K. Nørskov, I. Chorkendorff, The importance of surface morphology in controlling the selectivity of polycrystalline copper for CO_2 electroreduction, Phys. Chem. Chem. Phys. 14 (2012) 76–81.

[16] W. Ju, A. Bagger, G.-P. Hao, A.S. Varela, I. Sinev, V. Bon, B.R. Cuenya, S. Kaskel, J. Rossmeisl, P. Strasser, Understanding activity and selectivity of metal-nitrogen-doped carbon catalysts for electrochemical reduction of CO_2, Nat. Commun. 8 (2017) 944.

[17] K.B. Ibrahim, M.C. Tsai, S.A. Chala, M.K. Berihun, A.W. Kahsay, T.A. Berhe, W.N. Su, B.J. Hwang, A review of transition metal-based bifunctional oxygen electrocatalysts, J. Chin. Chem. Soc. 66 (2019) 829–865.

[18] B.A. Rosen, A. Salehi-Khojin, M.R. Thorson, W. Zhu, D.T. Whipple, P.J. Kenis, R.I. Masel, Ionic liquid–mediated selective conversion of CO_2 to CO at low overpotentials, Science (2011) 1209786.

[19] D.R. Kauffman, J. Thakkar, R. Siva, C. Matranga, P.R. Ohodnicki, C. Zeng, R. Jin, Efficient electrochemical CO_2 conversion powered by renewable energy, ACS Appl. Mater. Interfaces 7 (2015) 15626–15632.

[20] F.-X. Shen, J. Shi, T. -y. Chen, F. Shi, Q.-Y. Li, J.-Z. Zhen, Y.-F. Li, Y.-N. Dai, B. Yang, T. Qu, Electrochemical reduction of CO_2 to CO over Zn in propylene carbonate/tetrabutylammonium perchlorate, J. Power Sources 378 (2018) 555–561.

[21] N.S. Spinner, J.A. Vega, W.E. Mustain, Recent progress in the electrochemical conversion and utilization of CO_2, Catal. Sci. Technol. 2 (2012) 19–28.

[22] M.K. Birhanu, M.-C. Tsai, C.-T. Chen, A.W. Kahsay, T.S. Zeleke, K.B. Ibrahim, C.-J. Huang, W.-N. Su, B.-J. Hwang, Conversion of carbon dioxide into valuable chemicals through electrochemical reduction using transition metal electrocatalysts, meeting abstracts, Electrochem. Soc. (2019) 1090 1090.

[23] M. Nur Hossain, J. Wen & A. Chen, Unique copper and reduced graphene oxide nanocomposite toward the efficient electrochemical reduction of carbon dioxide Scientific Reports, 7 (2017) 1–10.

[24] S. Zhao, R. Jin, R. Jin, Opportunities and challenges in CO_2 reduction by gold-and silver-based electrocatalysts: from bulk metals to nanoparticles and atomically precise nanoclusters, ACS Energy Lett. 3 (2018) 452–462.

[25] K. Chen, X. Zhang, T. Williams, L. Bourgeois, D.R. MacFarlane, Electrochemical reduction of CO_2 on core-shell Cu/Au nanostructure arrays for syngas production, Electrochim. Acta 239 (2017) 84–89.

[26] P. De Luna, R. Quintero-Bermudez, C.-T. Dinh, M.B. Ross, O.S. Bushuyev, P. Todorović, T. Regier, S.O. Kelley, P. Yang, E.H. Sargent, Catalyst electro-redeposition controls morphology and oxidation state for selective carbon dioxide reduction, Nat. Catal. 1 (2018) 103.

[27] A.W. Kahsay, K.B. Ibrahim, M.-C. Tsai, M.K. Birhanu, S.A. Chala, W.-N. Su, B.-J. Hwang, Selective and low overpotential electrochemical CO₂ reduction to formate on CuS decorated CuO heterostructure, Catal. Lett. (2019) 1–10.

[28] Z.B. Hoffman, T.S. Gray, Y. Xu, Q. Lin, T.B. Gunnoe, G. Zangari, High Selectivity Towards Formate Production by Electrochemical Reduction of Carbon Dioxide at Copper–Bismuth Dendrites, ChemSusChem 12 (2019) 231–239.

[29] Z. Zhang, J. Xiao, X.J. Chen, S. Yu, L. Yu, R. Si, Y. Wang, S. Wang, X. Meng, Y. Wang, Reaction Mechanisms of Well-Defined Metal–N4 Sites in Electrocatalytic CO₂ Reduction, Angew. Chem. Int. Ed. 57 (2018) 16339–16342.

[30] J.E. Pander, M.F. Baruch, A.B. Bocarsly, Probing the mechanism of aqueous CO₂ reduction on post-transition-metal electrodes using ATR-IR spectroelectrochemistry, ACS Catal. 6 (2016) 7824–7833.

[31] L. Zhang, Z.J. Zhao, J. Gong, Nanostructured materials for heterogeneous electrocatalytic CO₂ reduction and their related reaction mechanisms, Angew. Chem. Int. Ed. Engl. 56 (2017) 11326–11353.

[32] M.K. Birhanu, M.-C. Tsai, A.W. Kahsay, C.-T. Chen, T.S. Zeleke, K.B. Ibrahim, C.-J. Huang, W.-N. Su, B.-J. Hwang, Copper and Copper-Based Bimetallic Catalysts for Carbon Dioxide Electroreduction, Adv. Mater. Interfaces 5 (2018) 1800919.

[33] Y.W. Choi, F. Scholten, I. Sinev, B. Roldan Cuenya, Enhanced stability and CO/formate selectivity of plasma-treated SnOₓ/AgOₓ catalysts during CO₂ electroreduction, J. Am. Chem. Soc. 141 (2019) 5261–5266.

[34] A.J. Garza, A.T. Bell, M. Head-Gordon, Mechanism of CO₂ reduction at copper surfaces: pathways to C₂ products, ACS Catal. 8 (2018) 1490–1499.

[35] J.L.L. Dong Dong Zhu, Shi Zhang Qiao, Recent advances in inorganic heterogeneous electrocatalysts for reduction of carbon dioxide, Adv. Mater. 28 (2016) 3423–3452.

[36] Y.-J. Zhang, V. Sethuraman, R. Michalsky, A.A. Peterson, Competition between CO₂ reduction and H₂ evolution on transition-metal electrocatalysts, ACS Catal. 4 (2014) 3742–3748.

[37] T.S. Zeleke, M.C. Tsai, M.A. Weret, C.J. Huang, M.K. Birhanu, T.C. Liu, C.P. Huang, Y.L. Soo, Y.W. Yang, W.N. Su, B.J. Hwang, Immobilized single molecular molybdenum disulfide on carbonized polyacrylonitrile for hydrogen evolution reaction, ACS Nano 13 (2019) 6720–6729.

[38] J. Durst, A. Siebel, C. Simon, F. Hasche, J. Herranz, H. Gasteiger, New insights into the electrochemical hydrogen oxidation and evolution reaction mechanism, Energy Environ. Sci. 7 (2014) 2255–2260.

[39] M.E. Scofield, Y. Zhou, S. Yue, L. Wang, D. Su, X. Tong, M.B. Vukmirovic, R.R. Adzic, S.S. Wong, Role of chemical composition in the enhanced catalytic activity of Pt-based alloyed ultrathin nanowires for the hydrogen oxidation reaction under alkaline conditions, ACS Catal. 6 (2016) 3895–3908.

[40] P. Hirunsit, W. Soodsawang, J. Limtrakul, CO₂ electrochemical reduction to methane and methanol on copper-based alloys: theoretical insight, J. Phys. Chem. C 119 (2015) 8238–8249.

[41] H. Lee, S.-K. Kim, S.H. Ahn, Electrochemical preparation of Ag/Cu and Au/Cu foams for electrochemical conversion of CO₂ to CO, J. Ind. Eng. Chem. 54 (2017) 218–225.

[42] A.A. Peterson, J.K. Nørskov, Activity descriptors for CO₂ electroreduction to methane on transition-metal catalysts, J. Phys. Chem. Lett. 3 (2012) 251–258.

[43] S.A. Chala, M.-C. Tsai, W.-N. Su, K.B. Ibrahim, A.D. Duma, M.-H. Yeh, C.-Y. Wen, C.-H. Yu, T.-S. Chan, H. Dai, B.-J. Hwang, Site activity and population engineering of niru-layered double hydroxide nanosheets decorated with silver nanoparticles for oxygen evolution and reduction reactions, ACS Catal. 9 (2018) 117–129.

[44] J.R. Dohyung Kim, Yi Yu, Abdullah Mohamed Asiri, Peidong Yang, Synergistic geometric and electronic effects for electrochemical reduction of carbon dioxide using gold–copper bimetallic nanoparticles, Nat. Commun. 5 (2014) 1–8.

[45] J. Christophe, T. Doneux, C. Buess-Herman, Electroreduction of carbon dioxide on copper-based electrodes: activity of copper single crystals and copper–gold alloys, Electrocatalysis 3 (2012) 139–146.

[46] Z.B. Hoffman, T.S. Gray, K.B. Moraveck, T.B. Gunnoe, G. Zangari, Electrochemical reduction of carbon dioxide to syngas and formate at dendritic copper–indium electrocatalysts, ACS Catal. 7 (2017) 5381–5390.

[47] Z. Xu, E. Lai, Y. Shao-Horn, K. Hamad-Schifferli, Compositional dependence of the stability of AuCu alloy nanoparticles, Chem. Commun. 48 (2012) 5626–5628.

[48] J. Jiao, R. Lin, S. Liu, W.-C. Cheong, C. Zhang, Z. Chen, Y. Pan, J. Tang, K. Wu, S.-F. Hung, Copper atom-pair catalyst anchored on alloy nanowires for selective and efficient electrochemical reduction of CO₂, Nat. Chem. 11 (2019) 222.

[49] M. Ma, H.A. Hansen, M. Valenti, Z. Wang, A. Cao, M. Dong, W.A. Smith, Electrochemical reduction of CO₂ on compositionally variant Au-Pt bimetallic thin films, Nano Energy 42 (2017) 51–57.

[50] Z.B. Hoffman, T.S. Gray, Y. Xu, Q. Lin, T.B. Gunnoe, G. Zangari, High selectivity towards formate production by electrochemical reduction of carbon dioxide at copper–bismuth dendrites, ChemSusChem 12 (2019) 231–239.

[51] E.P. George, D. Raabe, R.O. Ritchie, High-entropy alloys, Nat. Rev. Mater. 4 (2019) 515–534.

[52] J. Monzó, Y. Malewski, R. Kortlever, F.J. Vidal-Iglesias, J. Solla-Gullón, M. Koper, P. Rodriguez, Enhanced electrocatalytic activity of Au@ Cu core@ shell nanoparticles towards CO₂ reduction, J. Mater. Chem. A 3 (2015) 23690–23698.

[53] H.A. Hansen, J.B. Varley, A.A. Peterson, J.K. Nørskov, Understanding trends in the electrocatalytic activity of metals and enzymes for CO₂ reduction to CO, J. Phys. Chem. Lett. 4 (2013) 388–392.

[54] P. Grosse, D. Gao, F. Scholten, I. Sinev, H. Mistry, B. Roldan Cuenya, Dynamic changes in the structure, chemical state and catalytic selectivity of Cu nanocubes during CO₂ Electroreduction: size and support effects, Angew. Chem. 130 (2018) 6300–6305.

[55] S. Sarfraz, A.T. Garcia-Esparza, A. Jedidi, L. Cavallo, K. Takanabe, Cu–Sn bimetallic catalyst for selective aqueous electroreduction of CO₂ to CO, ACS Catal. 6 (2016) 2842–2851.

[56] G. b. Kovács, S.M. Kozlov, K.M. Neyman, Versatile optimization of chemical ordering in bimetallic nanoparticles, J. Phys. Chem. C 121 (2017) 10803–10808.

[57] J.-H. Kim, H. Woo, S.-W. Yun, H.-W. Jung, S. Back, Y. Jung, Y.-T. Kim, Highly active and selective Au thin layer on Cu polycrystalline surface prepared by galvanic displacement for the electrochemical reduction of CO₂ to CO, Appl. Catal. B: Environ. 213 (2017) 211–215.

[58] K. Ngamlerdpokin, N. Tantavichet, Electrodeposition of nickel–copper alloys to use as a cathode for hydrogen evolution in an alkaline media, Int. J. Hydrogen Energy 39 (2014) 2505–2515.

[59] X. Bai, W. Chen, C. Zhao, S. Li, Y. Song, R. Ge, W. Wei, Y. Sun, Exclusive formation of formic acid from CO₂ electroreduction by a tunable Pd-Sn alloy, Angew. Chem. 129 (2017) 12387–12391.

[60] D. Kim, C. Xie, N. Becknell, Y. Yu, M. Karamad, K. Chan, E.J. Crumlin, J.K. Nørskov, P. Yang, Electrochemical activation of CO₂ through atomic ordering transformations of AuCu nanoparticles, J. Am. Chem. Soc. 139 (2017) 8329–8336.

[61] L. Zhang, Z.J. Zhao, J. Gong, Nanostructured materials for heterogeneous electrocatalytic CO₂ reduction and their related reaction mechanisms, Angew. Chem. Int. Ed. 56 (2017) 11326–11353.

[62] D.-Y. Wang, M. Gong, H.-L. Chou, C.-J. Pan, H.-A. Chen, Y. Wu, M.-C. Lin, M. Guan, J. Yang, C.-W. Chen, Highly active and stable hybrid catalyst of cobalt–doped FeS₂ nanosheets–carbon nanotubes for hydrogen evolution reaction, J. Am. Chem. Soc. 137 (2015) 1587–1592.

[63] M.R. Singh, E.L. Clark, A.T. Bell, Effects of electrolyte, catalyst, and membrane composition and operating conditions on the performance of solar-driven electrochemical reduction of carbon dioxide, Phys. Chem. Chem. Phys. (2015) 1–29.

[64] T.E.L. Eric J. Dufek, M.E. McIlwain, Influence of electrolytes and membranes on cell operation for syn-gas production, Electrochem. Solid-State Lett. 15 (2012) B48–B50.

[65] I. Merino-Garcia, E. Alvarez-Guerra, J. Albo, A. Irabien, Electrochemical membrane reactors for the utilisation of carbon dioxide, Chem. Eng. J. 305 (2016) 104–120.

[66] M.R. Singh, E.L. Clark, A.T. Bell, Effects of electrolyte, catalyst, and membrane composition and operating conditions on the performance of solar-driven electrochemical reduction of carbon dioxide, Phys. Chem. Chem. Phys. 17 (2015) 18924–18936.

[67] B. Domènech, V. Romero, M.I. Vázquez, M. Avila, J. Benavente, M. Muñoz, J. Macanás, Chemical and electrochemical characterization of Nafion containing silver nanoparticles in a stripe-like distribution, RSC Adv. 6 (2016) 9923–9931.

[68] M.S. McGovern, E.C. Garnett, C. Rice, R.I. Masel, A. Wieckowski, Effects of Nafion as a binding agent for unsupported nanoparticle catalysts, J. Power Sources 115 (2003) 35–39.

[69] B.-J. Hwang, L.S. Sarma, J.-M. Chen, C.-H. Chen, S.-C. Shih, G.-R. Wang, D.-G. Liu, J.-F. Lee, M.-T. Tang, Structural models and atomic distribution of bimetallic nanoparticles as investigated by X-ray absorption spectroscopy, J. Am. Chem. Soc. 127 (2005) 11140–11145.

[70] C.H. Chen, C.J. Pan, W.N. Su, L.S. Sarma, C.C.A. Andra, H.S. Sheu, D.G. Liu, J.F. Lee, B.J. Hwang, Unravelling surface composition of bimetallic nanoparticles, ChemNanoMat 2 (2016) 117–124.

[71] C.X. Dohyung Kim, Nigel Becknell, Yi Yu, Mohammadreza Karamad, Karen Chan, Ethan J. Crumlin, Jens K. Nørskov, Peidong Yang, Electrochemical activation of CO₂ through atomic ordering transformations of AuCu nanoparticles, Am. Chem. Soc. 139 (2017) 8329–8336.

[72] I.A. Safo, F. Liu, K. Xie, W. Xia, Oxidation and stability of multi-walled carbon nanotubes in hydrogen peroxide solution, Mater. Chem. Phys. 214 (2018) 472–481.

[73] V. Datsyuk, M. Kalyva, K. Papagelis, J. Parthenios, D. Tasis, A. Siokou, I. Kallitsis, C. Galiotis, Chemical oxidation of multiwalled carbon nanotubes, Carbon N Y 46 (2008) 833–840.

[74] I.D. Rosca, F. Watari, M. Uo, T. Akasaka, Oxidation of multiwalled carbon nanotubes by nitric acid, Carbon N Y 43 (2005) 3124–3131.

[75] A.P. Grosvenor, B.A. Kobe, M.C. Biesinger, N.S. McIntyre, Investigation of multiplet splitting of Fe 2p XPS spectra and bonding in iron compounds, Surf. Interface Anal. 36 (2004) 1564–1574.

[76] B.D.G. Michael Bancroft, David K. Creber, Shake-up satellite structure in the X-ray photoelectron spectra (ESCA) of metal hexacarbonyls, Inorg. Chem. 17 (1978) 1008–1013.

[77] S.L. Petter Persson, Abraham Szoke, Beata Ziaja, Janos Hajdu, Shake-up and shake-off excitations with associated electron losses in X-ray studies of proteins, Protein Sci. 10 (2001) 2480–2484.

[78] K.P. Kuhl, T. Hatsukade, E.R. Cave, D.N. Abram, J. Kibsgaard, T.F. Jaramillo, Electrocatalytic conversion of carbon dioxide to methane and methanol on transition metal surfaces, J. Am. Chem. Soc. 136 (2014) 14107–14113.

[79] S. Ma, M. Sadakiyo, R. Luo, M. Heima, M. Yamauchi, P.J. Kenis, One-step electrosynthesis of ethylene and ethanol from CO_2 in an alkaline electrolyzer, J. Power Sources 301 (2016) 219–228.

[80] D.D. Zhu, J.L. Liu, S.Z. Qiao, Recent advances in inorganic heterogeneous electrocatalysts for reduction of carbon dioxide, Adv. Mater. 28 (2016) 3423–3452.

[81] C.S. Joseph H. Montoya, Karen Chan, Jens K. Nørskov, Theoretical Insights into a CO Dimerization Mechanism in CO_2 Electroreduction, J. Phys. Chem. Lett. 6 (2015) 2032–2037.

[82] F. Calle-Vallejo, Marc T.M. Koper, Theoretical Considerations on the Electroreduction of CO to C2 Species on Cu(100) Electrodes, Angew. Chem. 125 (2013) 7423–7426.

[83] M.K. Birhanu, A.W. Kahsay, C.-T. Chen, T.S. Zeleke, K.B. Ibrahim, C.-J. Huang, W.-N. Su, B.-J. Hwang, Copper and Copper-Based Bimetallic Catalysts for Carbon Dioxide Electroreduction, Adv. Mater. Interfaces 5 (2018) 1800919.